

Augmenting the Leidenfrost Temperature of Droplets via Nanobubble Dispersion

Gudlavalleti V V S Vara Prasad, Harsh Sharma, Neelkanth Nirmalkar, Purbarun Dhar,* and Devranjan Samanta*



Cite This: *Langmuir* 2022, 38, 15925–15936



Read Online

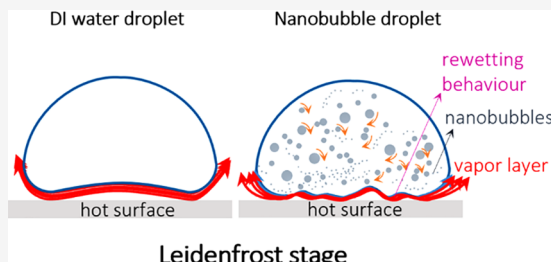
ACCESS |

Metrics & More

Article Recommendations

Supporting Information

ABSTRACT: Droplets may rebound/levitate when deposited over a hot substrate (beyond a critical temperature) due to the formation of a stable vapor microcushion between the droplet and the substrate. This is known as the Leidenfrost phenomenon. In this article, we experimentally allow droplets to impact the hot surface with a certain velocity, and the temperature at which droplets show the onset of rebound with minimal spraying is known as the dynamic Leidenfrost temperature (T_{DL}). Here we propose and validate a novel paradigm of augmenting the T_{DL} by employing droplets with stable nanobubbles dispersed in the fluid. In this first-of-its-kind report, we show that the T_{DL} can be delayed significantly by the aid of nanobubble-dispersed droplets. We explore the influence of the impact Weber number (We), the Ohnesorge number (Oh), and the role of nanobubble concentration on the T_{DL} . At a fixed impact velocity, the T_{DL} was noted to increase with the increase in nanobubble concentration and decrease with an increase in impact velocity for a particular nanobubble concentration. Finally, we elucidated the overall boiling behaviors of nanobubble-dispersed fluid droplets with the substrate temperature in the range of 150–400 °C against varied impact We through a detailed phase map. These findings may be useful for further exploration of the use of nanobubble-dispersed fluids in high heat flux and high-temperature-related problems and devices.



1. INTRODUCTION

The Leidenfrost effect is the phenomenon wherein a droplet levitates above its vapor cushion, formed on a substrate heated to a temperature sufficiently high above the saturation temperature.^{1,2} The heat transfer rate substantially drops in the Leidenfrost state as the vapor cushion is a bad conductor of heat. Discovered by (in the vicinity of the 1750s) a German doctor, Johann Gottlob Leidenfrost,³ the phenomenon holds significance in modern applications involving liquid–vapor phase changes and multiphase thermohydrodynamics. In today's world, the Leidenfrost effect is of prime concern for the safety and management of nuclear reactors and power plant systems. Also, the study of droplet impact on heated substrates is useful in the optimal performance of myriad applications such as spray cooling in fire fighting, sprinkling, electronic cooling,⁴ combustion dynamics of direct fuel injection,⁵ drag reduction,⁶ and directed motion.⁷ Thus, the Leidenfrost effect also holds importance in droplet, spray, and jet impingement systems operating at high temperatures.

With the advancements in high-speed photography, laser-based optical diagnostics, and interferometry, experimentalists have been able to unravel various features of the Leidenfrost dynamics. Self-propulsion dynamics of drops of various sizes at high temperatures (~300 °C) was explored using particle image velocimetry.⁸ The vorticity distribution within the drop was noted to vary depending upon the capillary length scale of

the fluid. Droplets with a diameter less than the capillary length of the droplet fluid showed the existence of one vorticity, whereas larger droplets displayed the existence of two internal vortices. Also, it was shown that propulsion mobility is dependent on the droplet size. The dynamics of the self-propelling droplets may be due to the vapor film whose flow can entrain fluid due to the viscous effect as well as the thermal-gradient-induced Marangoni effect.⁹ Star-shaped droplets with arms (four, six, or eight) were observed in the Leidenfrost state. The formation of these transient states was attributed to the Faraday instability triggered by the vibrations of the vapor cushion.¹⁰ Tran et al.¹¹ performed interferometry measurements to reveal the structure of the vapor layer beneath the droplets. They showed that the nondimensional maximum spreading diameter during gentle and spray boiling regimes scales with the Weber number ($\sim We^{0.4}$), which is steeper than the power-law scaling at ambient temperatures ($\sim We^{0.25}$).

Received: July 18, 2022

Revised: November 24, 2022

Published: December 12, 2022



An enhancement of the Leidenfrost point or temperature (LFT) can be achieved by various methods, viz., the dispersion of polymer additives,^{12,13} surfactants,^{14,15} or nanoparticles.^{16,17} Other avenues of LFT enhancement were achieved by substrate modification using femtosecond laser-based surface processing^{18,19} or by the use of an electric field.²⁰ The aim of this paper is to augment the LFT of fluids by generating and dispersing stable nanobubbles (NB) in the fluid. Fluid dispersions of nanobubbles have recently been in the limelight^{21–25} due to their potential in water treatment, food processing, and sonochemistry.

The nanobubbles possess a high surface to volume ratio (the ratio varies as $6/d$ for spherical shapes, where d is diameter) and a high mass-transfer coefficient. The surface zeta potential²³ of nanobubble dispersions is observed to be approximately -33 mV, which is well within the colloidal stability regime of nanosuspensions. One of the peculiar properties of nanobubbles is extra longevity and thermodynamic and colloidal phase stability, and it has been experimentally shown that nanobubble dispersions can be stable for more than 2–4 months.²²

According to Epstein and Plesset's theory,²⁶ the lifetime²⁷ of a bubble is expressed as

$$t_f = \frac{R^2 \rho_g}{2C_s(1-f)} \quad (1)$$

where t_f , R , ρ_g , C_s , and f represent the lifetime of the bubble, radius of the bubble, density of the gas bubble, saturation concentration, and gas saturation ratio, respectively. For nanobubbles,²⁸ the lifetime is on the order of microseconds (for ~ 100 –200-nm-diameter bubbles dispersed in water, $t_f = 20$ –80 μ s), considering that Henry's law and the Young–Laplace equation are valid at the nanoscale. In stark contrast, multiple experimental results show evidence of the existence of nanobubbles^{22–24} for a very long time. The extra longevity of nanobubbles is still puzzling, and there is no universal theory to explain the behavior of nanobubbles. Some recent works demonstrated that the ion enrichment at the interface may plausibly be responsible for such extraordinary stability.²²

The extra longevity and homogeneously dispersed gaseous phase ensure that nanobubble dispersions have several utilities, such as wastewater treatment,²⁹ ultrasound contrast agents,³⁰ therapeutic drug delivery,³¹ drag reduction in microchannels,³² promotion of the physiological activity of living organisms,³³ enhanced germination rate of seeds,³⁴ and improved blood oxygenation.³⁵ In this work, we explore how dispersions of nanobubbles in liquids may augment the dynamic LFT of the fluid. We test the premise using deionized water-based stable nanobubble dispersions and experimentally explore the droplet impact of Leidenfrost dynamics. We further direct the study toward understanding the effect of governing parameters, viz., nanobubble concentration, impact Weber number We , and Ohnesorge number Oh , and determine their roles toward the Leidenfrost behavior and other boiling regimes.

2. MATERIALS AND METHODOLOGIES

2.1. Experimental Setup. The schematic view of the experimental setup used in this study is illustrated in Figure 1. The setup is similar to our previous reports on Leidenfrost dynamics.^{13–15} We have utilized a programmable hot plate (Holmarc Opto-Mechtronics Ltd., India) with a digitized temperature controller to heat the substrate to temperatures ranging from 150 to 350 °C and to maintain near-isothermal conditions on the substrate during the

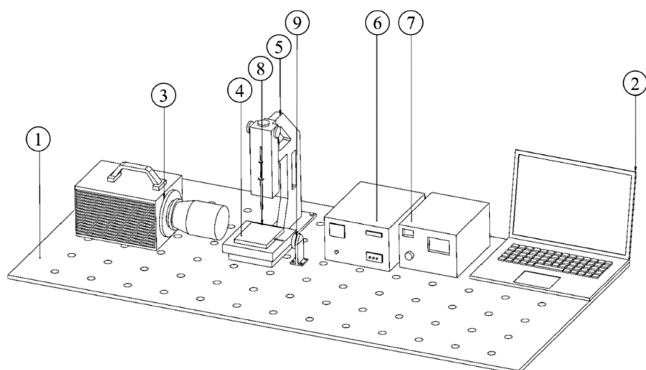


Figure 1. Schematic of the experimental setup: (1) vibration-free table top, (2) computer for data acquisition and camera control, (3) high-speed camera with a macrolens, (4) hot substrate, (5) droplet-dispersing mechanism (DDM) unit, (6) DDM and backlight illumination controller, (7) hot substrate temperature controller, (8) microsyringe, and (9) backlight array.

experiments. In this study, a square stainless-steel plate (80 mm × 180 mm) mounted on the heating element was used as the substrate. A T-type thermocouple probe was inserted into the stainless-steel hot plate. The thermocouple measures the temperature of the substrate ~ 1 mm below the top surface (where the droplet impacts) and is connected to the programmable temperature controller. The controller maintains the hot plate temperature at nearly isothermal conditions (± 2 to 3 °C deviations from the set temperature data point).

A height-alterable droplet dispenser coupled with a digitized controller unit has been used to generate and release the droplets from different heights. As similar to our previous studies,^{15,36} we have performed experiments at different Weber numbers ($We = \frac{\rho U^2 D_o}{\sigma}$), i.e., the ratio of inertial forces to surface tension forces, and Ohnesorge numbers ($Oh = \frac{\mu}{\sqrt{(\rho \sigma D_o)}} = \frac{\sqrt{We}}{Re}$) i.e., the ratio of viscous forces to both inertial and capillary forces, where ρ , U , D_o , and σ represent the density, impact velocity, preimpact droplet diameter, and surface tension of the fluid, respectively. The Reynolds number is denoted as Re in the definition of the Ohnesorge number. The Weber number We is changed by altering the heights to obtain different impact velocities.

A microsyringe (± 0.1 μ L volumetric accuracy) attached to the droplet dispenser is used to dispense fluid droplets of the required volume through a flat head steel needle (22 gauge). In this study, we have utilized a high-speed camera (Photron, U.K.) to capture the droplet impact hydrodynamic events during the Leidenfrost stage. All experiments were recorded at 4000 frames/s at 1024×1024 resolution using a macrolens (Nikon) with a constant focal length of 105 mm. Before each experiment, the stainless-steel substrate was cleaned with deionized water followed by acetone to remove the dirt particles and contaminants from the hot surface. The heater was heated to a set temperature data point and allowed to attain a steady state, and then each impact experiment was conducted.

2.2. Nanobubble Generation. In this study, we used nanobubble-dispersed deionized (DI) water as the test fluid. Nanobubbles are ultrafine bubbles with diameters in the submicrometer range and a mean diameter ranging from 100 to 200 nm.²⁸ Oxygen nanobubbles are generated using the nanopore gas diffusion method in deionized water as shown in Figure 2a.³⁷ High-pressure oxygen gas was introduced through nanopores, and nanobubbles were generated due to the shear force exerted by the water flowing in a millichannel in a cross-flow configuration. The volumetric flow rate of gas and pressure play an important role in controlling the mean diameter of nanobubbles and the concentration of nanobubbles. The optimum flow rate and gas pressure used in this work are 2 L/min and 3 bar,

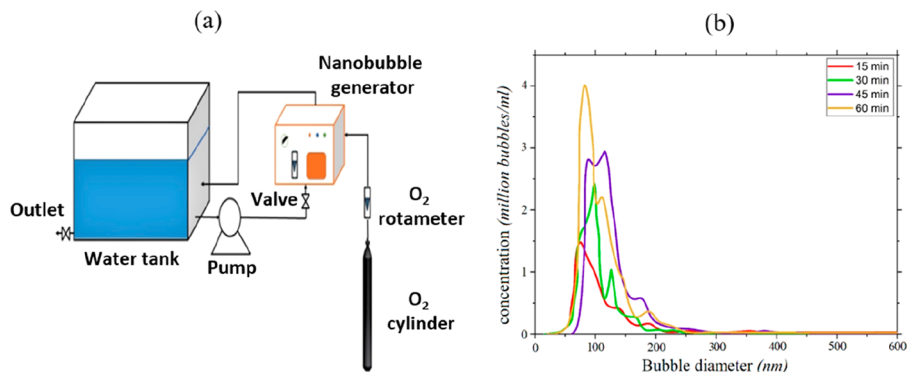


Figure 2. (a) Experimental setup for nanobubble generation and (b) bubble size distribution at different time intervals.

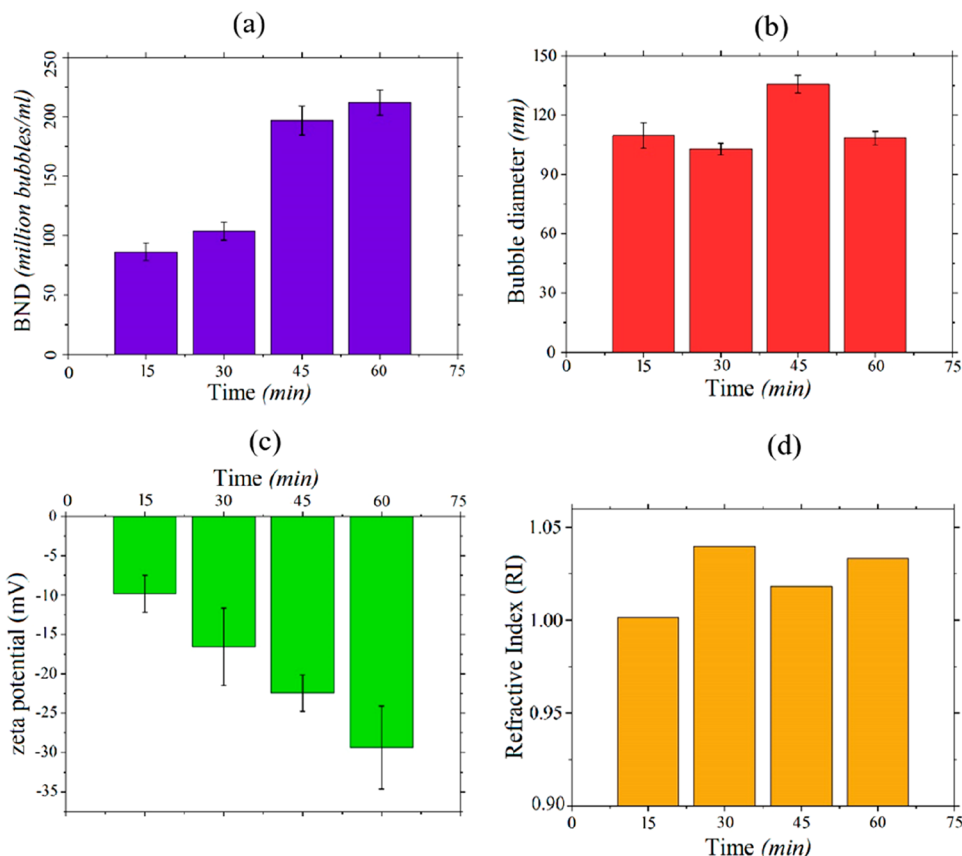


Figure 3. Bulk nanobubbles generated at time intervals of 15, 30, 45, and 60 min. (a) Bubble number density (BND), (b) bubble diameters, (c) zeta potential, and (d) refractive index.

respectively. The experimental set was run for 60 min only as there is no further significant increase in the concentration.

NTA (nanoparticle tracking analysis) and DLS (dynamic light scattering) were used to characterize the nanobubble sample under atmospheric conditions.³⁸ The results were presented in terms of the bubble size distribution, concentration of nanobubbles, bubble diameters, and zeta potential. The concentration of nanobubbles increases monotonically with time, and the mean diameter lies in the range of 100–120 nm as shown in Figure 2b. The maximum concentration of nanobubbles occurs at 60 min with 214 million bubbles/mL whereas the mean diameter is observed in the range of 100–140 nm, as shown in Figure 3a,b, respectively. The nanobubbles are observed to have a negative zeta potential of –28 mV as shown in Figure 3c. The high negative zeta potential around the nanobubbles helps make them stable in suspension for a longer time, leading to long-term stability.

Bubble generation was performed carefully to avoid contamination in the liquid. The source of the contamination could be the metals used in the nanobubble generator. The refractive index of nanobubbles is estimated in order to identify the possible chances of contamination. Evidently, the refractive index of solid particles and drops must always be higher than 1.33, while the refractive index of nanobubbles lies close to 1. We have calculated the refractive index of nanobubbles using the Mie scattering theory method²¹ based on the scattering intensity measurement. Clearly, the refractive index of nanobubbles in all cases, as shown in Figure 3d, was very close to 1 (RI of air = 1), which confirms that these are gas nanobubbles.

In this study, different concentrations of oxygen gas nanobubble-dispersed solutions were used to generate droplets. Thermophysical properties such as the density, surface tension, and viscosity of the test solutions significantly vary with increasing oxygen nanobubble concentration. Increases in the concentration of solid particles will lead to increases in viscosity. However, increases in the concentration

of nanobubbles may not necessarily lead to increases in viscosity. The increase in the liquid–gas interface due to the increase in NB concentration in the bulk of the liquid leads to increased slip between surfaces; therefore, the measured shear force decreases in nanobubble suspensions.³⁹ The decreasing trend in density with increasing NB concentration is obvious due to the increase in the gaseous phase in the NB fluids. Surface tension is the tangential force acting on the interface per unit length that can also be expressed by the Gibbs free energy per unit area at constant temperature and pressure. Clearly, the Gibbs free energy is expected to be at a minimum both in the bulk and in the interface of the system at thermodynamic equilibrium. The interfacial area of the system boundary may increase by the migration of nanobubbles toward the interface. Therefore, nanobubbles contribute to a decrease in the surface tension.

We adopted the Wilhelmy plate method to measure the surface tension of the test fluids at 25 °C. All of the thermophysical properties of nanobubble-dispersed fluid solutions have been reported in Table 1.

Table 1. Thermophysical Properties of Test Fluid Droplets at 25 °C^a

nанобubble concentration (million bubbles/mL)	D _o	ρ	σ	η	λ _c
0	2.6	995.6	71.8	0.8	2.7
87	2.6	993.3	69.9	0.9	2.6
104	2.8	992.7	68.1	0.8	2.6
158	2.8	992.2	66.7	0.8	2.6
214	2.9	991.2	62.3	0.8	2.5

^aPreimpact droplet diameter D_o (mm), density ρ (kg/m³), surface tension σ (mN/m), viscosity η (mPa·s), and capillary length λ_c (mm).

3. RESULTS AND DISCUSSION

In this section, we discuss the impact hydrodynamics of the nanobubble dispersion droplets over hot surfaces with varying impact Weber numbers (We). The different regimes of boiling

and the phenomenology of nanobubble dispersion droplets are discussed one after another.

3.1. Contact Boiling Regime ($T_s \approx 150$ °C) < T_{DL} . Figure 4 illustrates temporal snapshots of the droplets with different nanobubble concentrations at a fixed impact velocity of $U = 0.5$ m/s. The advection of the bubbles in NB fluid droplets was observed inside liquid droplets during the contact boiling [$(T_s \approx 150$ °C) < T_{DL}] stage. In Figure 4, it has been noticed that no such advective motion exists in the case of deionized water droplets and that the dissolved oxygen nanobubbles coalesce and transform into larger bubbles in the lower half of the droplet adjacent to the heated substrate. (See the third column of the second, third, and fourth rows of Figure 4.) Subsequently, due to buoyancy and the thermal Marangoni effect due to the surface tension gradient induced by the temperature variation existing between the heated droplet bottom surface and the relatively less heated top portion,^{39,40} these bubbles travel in a vertical direction away from the heated surface. It is also noticed that the vigorousness of the advective motion of the bubbles is enhanced with an increase in nanobubble concentration (Supporting Information videos).

Diwater droplets exhibit the contact boiling (first row and columns three through five of Figure 4) phenomenon through bulging its volume up to a contact time of 107.5 ms. The contact boiling was followed by nucleate boiling due to the vigorous nucleation of vapor bubbles beneath the droplet. Unlike DI water droplets, the nanobubble-dispersed fluid droplets interestingly exhibit CCR (constant contact radius) mode (see columns three through five of the NB fluid droplets in Figure 4) with no shift of its triple line during boiling. This behavior is analogous to the constant contact radius mode observed in the evaporation of droplets.^{41–43} On further magnification of Figure 4 (second row and columns three through five in the top row of Figure 4), it is readily evident that the nanobubble fluid droplets are in CCR mode via the

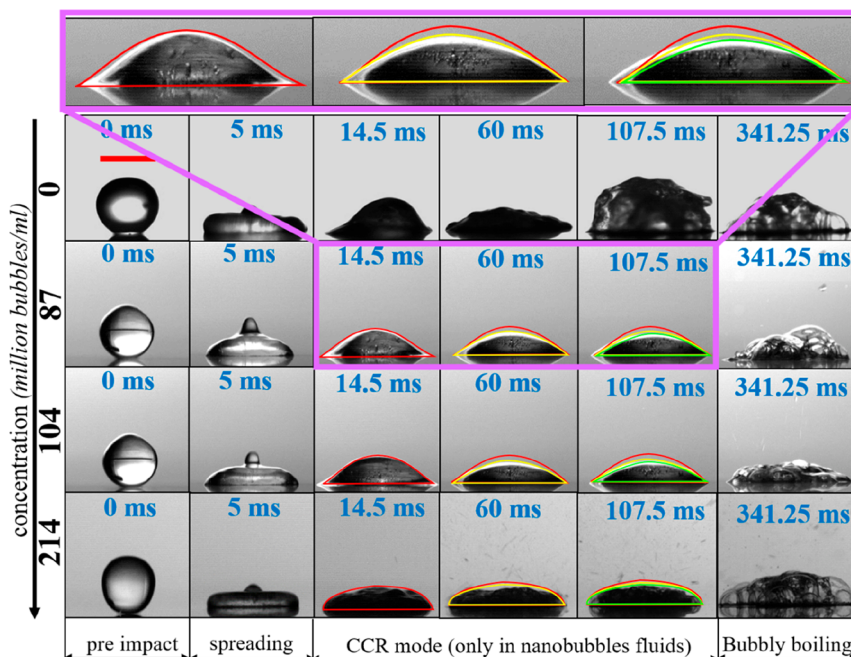


Figure 4. Temporal evolution of the droplet during the contact boiling stage, i.e., at ($T_s \approx 150$ °C) < T_{DL} at a fixed impact velocity of $U = 0.5$ m/s. The violet color inset represents the CCR mode of NB fluids in Figure 4. The Supporting Information movies of water (Video S2) and 104 million bubbles/mL (Video S1) drops illustrate the CCR mode in the case of NB fluids.

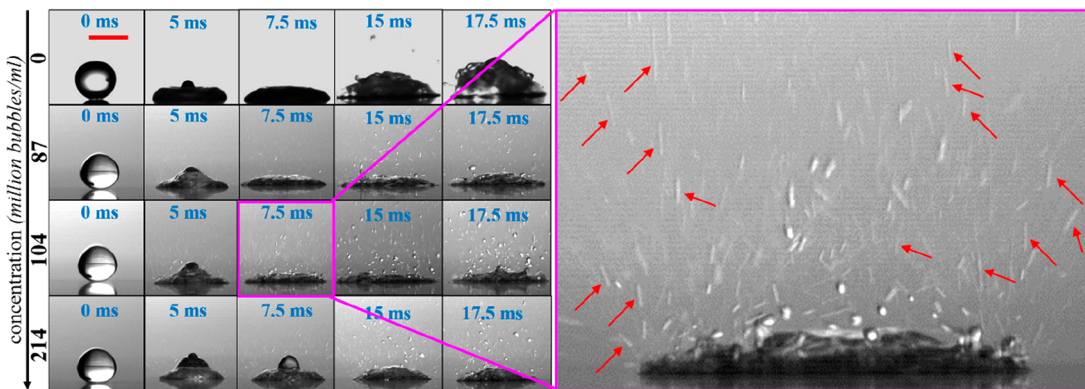


Figure 5. Temporal snapshots of the splashing behavior associated with thin jet ejection during the transition boiling stage, i.e., at ($T_s \approx 190^\circ\text{C}$) $< T_{DL}$ at a fixed impact velocity of $U = 0.5 \text{ m/s}$. The red arrow in the inset represents the jet ejection along with spraying. A Supporting Information video (Video S3) is added for further clarity.

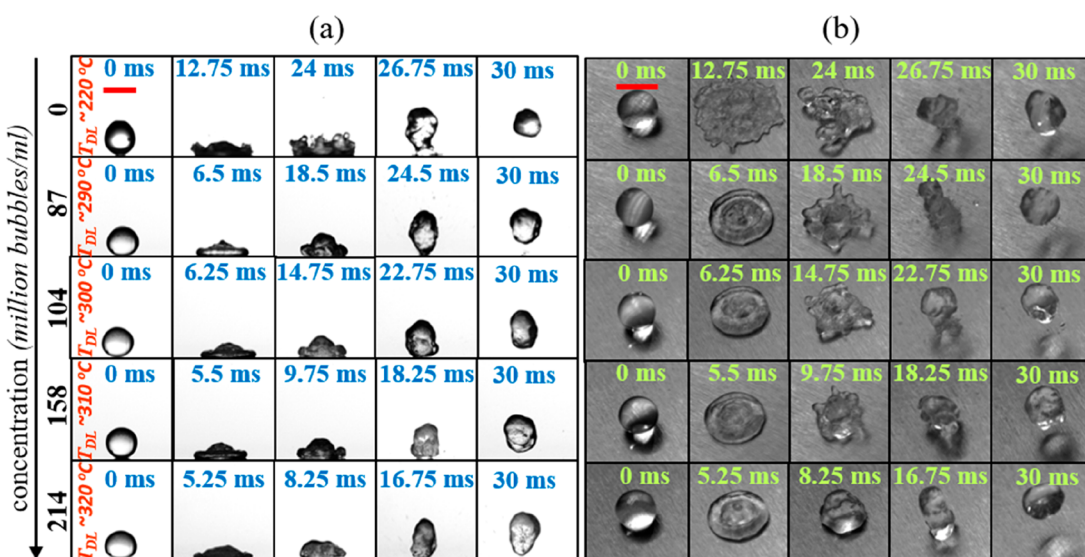


Figure 6. Influence of nanobubble concentration on T_{DL} : temporal evolution (a) side views and (b) top views of impacting droplets with a low impact velocity of $U = 0.5 \text{ m/s}$ at their respective T_{DL} values. The scale bar represents 2.64 mm and is the same for all cases. The first row with 0 million bubbles/mL shows water droplets, and nanobubble dispersion concentration increases from top to bottom. (The arrow at the extreme left shows concentration values.)

change in their contact angle (red, yellow, and green droplet curvature profiles in the inset of Figure 4) without losing their pinning effect. The CCR mode lasted for ~ 245 ms for 87 million and 104 million bubbles/mL. However, for higher NB concentration (i.e., 214 million bubbles/mL), each droplet displays CCR mode along with the ejection of secondary droplets. Eventually, this nanobubble fluid droplet enters the contact boiling stage and transforms to bubbly boiling (nucleate boiling) with increasing time.

3.2. Transition Boiling Regime ($T_s \approx 190^\circ\text{C}$) $< T_{DL}$. Next, we shift our focus to the splashing behavior of droplets during transition boiling [$(T_s \approx 190^\circ\text{C}) < T_{DL}$]. The splashing behavior of impinging droplets of both water and NB solutions is illustrated in Figure 5, where it has been noticed that all deionized water droplets show the usual secondary droplet atomization during transition boiling due to the onset of the coalescence of the vapor bubbles of the liquid beneath the droplet. However, in the case of droplets with NB solutions, droplets display the vigorous ejection of thin cylindrical jets or elongated secondary droplets (red arrows in Figure 5). No such onset of thin cylindrical jet ejection was observed in the

case of pure deionized water droplets. With increases in contact time as well as NB concentration, the vigorousness of this thin jet ejection is increased.

3.3. Dynamic Leidenfrost Effect ($T_s \approx T_{DL}$). Next, we shift our attention to the major focus of the present work: understanding how the presence of nanobubbles affects the droplet Leidenfrost regime. The substrate temperature at which the droplet exhibits the onset of rebound with minimal spraying is noted as the dynamic Leidenfrost temperature (T_{DL}).^{13,15} Figure 6a,b illustrates the temporal evolution of NB droplets of different concentrations and their corresponding dynamic Leidenfrost temperature T_{DL} at a fixed impact velocity of $U = 0.5 \text{ m/s}$. In the first column of Figure 6a, it is evident that the increase in nanobubble concentration leads to an increase in T_{DL} at $U = 0.5 \text{ m/s}$. Compared to pure DI water, the increase in T_{DL} was as high as $\sim 100^\circ\text{C}$ for this same impact velocity (fourth and fifth rows of Figure 6). For all of the ranges of impact velocities tested, at any fixed velocity, the T_{DL} was observed to increase monotonically with an increase in nanobubble concentration (Figure 7). At a fixed nanobubble concentration, the T_{DL} decreased with the increase in impact

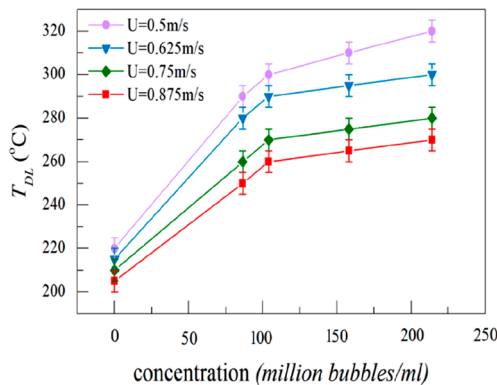


Figure 7. Effect of droplet impact velocity on dynamic Leidenfrost temperature (T_{DL}) for different nanobubbles concentrations. The error bars represent a variation of ± 5 °C.

velocity. Contrary to the previous studies where fizzy (carbonated) droplets levitated on superhydrophobic surfaces at ambient temperature⁴⁴ and the Leidenfrost temperature decreased with increasing dissolved gas concentration in water,⁴⁵ the oxygen nanobubbles of the NB fluids alter the T_{DL} in a counterintuitive manner.

A recent study⁴⁶ has shown that near the transition Leidenfrost point, oscillatory boiling occurs. Oscillatory boiling signifies the alternate occurrence of boiling and rewetting over time. The study reports the rewetting velocity of the form

$$v_{re} = \left(\frac{P_v - P_l}{4\rho_l F} \right)^{1/2} \quad (2)$$

Here, P_v and P_l are the pressure inside the embryonic vapor bubble and the liquid pressure, respectively. ρ_l is the liquid density, and F is a correction factor for the partial spherical shape of the vapor embryo. P_v is estimated as

$$P_v = P_{sat}(T_l) \exp \frac{v_l \{ P_l - P_{sat}(T_l) \}}{RT_l} \quad (3)$$

where P_{sat} is the saturation pressure at liquid temperature T_l and v_l is the specific volume of the liquid. We have taken $T_l = 200$ °C as a reference since for water T_{DL} was observed at temperatures of as high as ~220 °C. Now, at $T_l = 200$ °C we

have taken the saturation pressure and specific volume from steam tables and estimated the rewetting velocity as ~16.23 m/s. This is the same order of magnitude as in the reported study.⁴⁶ Similarly for NB fluids, the highest T_{DL} was observed at ~320 °C. Hence $T_l = 300$ °C was taken as a reference point. For $T_l = 300$ °C, the rewetting value is a complex number since P_l (1 atm pressure) is less than P_v . Hence, the unrealistic value is an indicator that for water, 300 °C is already past the Leidenfrost state and is not in the oscillatory phase.

We hypothesize that for NB fluids the nanobubbles act as the embryos for the nucleation sites. If we consider the physical properties of the NB fluid (214 millions/mL) from Table 1 and the mean NB radius to be 100 nm (refer Figure 2b), then by using the Laplace equation $\Delta p = \frac{2\sigma}{r}$ we can substitute the Δp value into the equation of v_{re} and get a realistic value of 20 m/s. We can hypothesize that due to the higher pressure difference within the bubble and the liquid there exists a realistic possibility for rewetting to happen, which basically disrupts continuous vapor formation and thereby causes a higher T_{DL} . We further theorize that upon contact of the NB fluid droplet with the superheated surface, the nanobubbles at and near the liquid–solid interface are thermally destabilized and expand rapidly. This leads to the release of the gas from the nanobubbles at and near the heated interface, leading to the formation of a micrometer-scale thin gas layer between the NB droplet and the heated surface. We hypothesize that this gas layer reduces the effective contact area between the droplet and the hot surface, thereby delaying the formation of the stable vapor cushion which signifies the onset of the Leidenfrost regime.

3.4. Scaling T_{DL} with Weber (We) and Ohnesorge (Oh) Numbers.

In this section, we have presented the scaling relations of T_{DL} with two different nondimensional parameters: the Weber number ($We = \frac{\rho U^2 D_o}{\sigma}$) and the Ohnesorge number ($Oh = \frac{\mu}{\sqrt{(\rho \sigma D_o)}} = \frac{\sqrt{We}}{Re}$). Physically, the Weber number represents the ratio of inertial force to surface tension. Figure 8a exhibits the decreasing trend in the T_{DL} with increasing impact We for a fixed nanobubble concentration ($T_{DL} \approx We^{-0.15}$). The decreasing trend in T_{DL} with an increase in the Weber number is similar to the Leidenfrost phenomenon studies for polymer

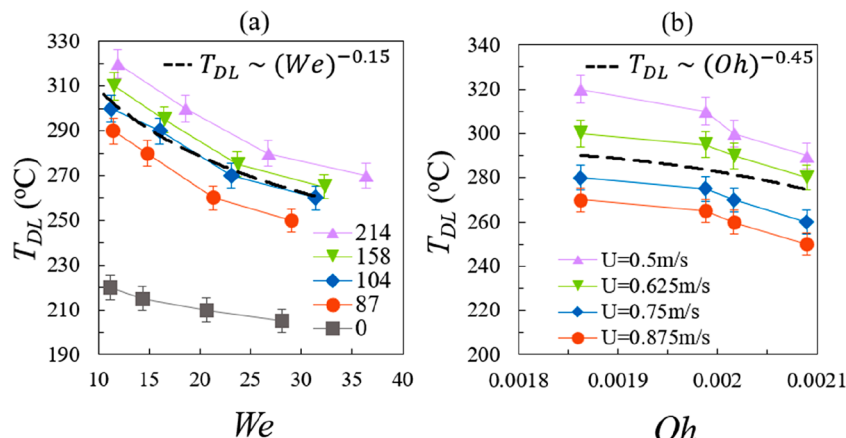


Figure 8. Relationship of T_{DL} with (a) We (legend values represent million bubbles/mL; for instance, 214 represents a fluid with a dissolved oxygen nanobubble concentration of 214 million bubbles/mL) and (b) Oh for different nanobubble concentrations. The dashed lines represent the scaling relationships obtained from the data. The lowest Oh value is for an NB fluid of 214 million bubbles/mL whereas the highest Oh value is for water.

droplets¹³ and surfactant droplets.¹⁵ At higher We , due to higher inertia, drops attain higher spreading. Due to the higher area of contact between the spreading droplet and heated substrate, a higher proliferation of nucleation sites at the fluid–solid interface leads to quicker vapor formation. The augmented rate of vapor layer formation leads to droplet rebound at lower temperature and consequently the T_{DL} .

For the same We , the T_{DL} increases with the increase in NB concentration. With the change in NB concentration, there are changes in material properties such as the density, viscosity, surface tension, and drop equilibrium size. Consequently, we need another nondimensional number, i.e., the Ohnesorge number (Oh), which represents the ratio of viscous force to both inertial and surface tension forces. To elucidate the role of viscous effects, we have probed the dependence of T_{DL} on the Ohnesorge number in Figure 8b. It must be noted that Oh is lowest for the highest-concentration NB fluid ($Oh \approx 0.00186$) and highest for DI water ($Oh \approx 0.0021$). For a fixed NB fluid, the T_{DL} decreases with increasing velocity. This observation is in agreement with Figure 7. For a fixed-impact velocity, T_{DL} decreased with an increase in Oh and follows the scaling relationship $T_{DL} \approx Oh^{-0.45}$.

Analogous to our previous study of Leidenfrost phenomena with surfactant droplets,¹⁵ we have attempted to elucidate the effect of all responsible forces of the NB fluid droplets, and we introduced a scaling relationship by combining nondimensional numbers We and Oh through least-squares regression. We illustrated the scaling relationship with experimental data points (T_{DL}) against the calculated data (fitted value of the scaling relation) (T_{DL}) in Figure 9. The experimental results of

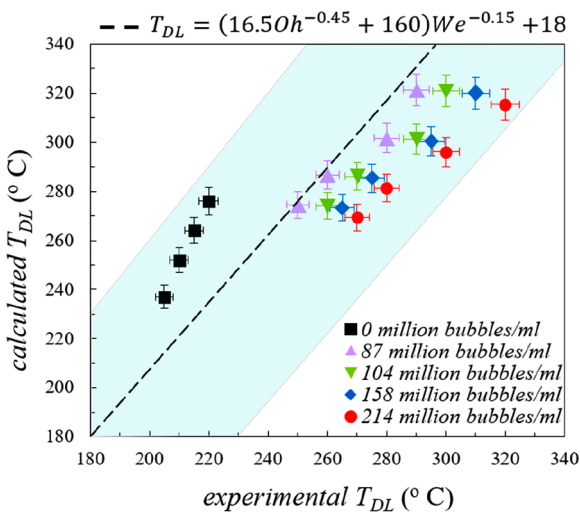


Figure 9. Scaling correlation between the experimental and calculated T_{DL} values of various nanobubbles concentrations.

T_{DL} are fitted according to the following pattern: $T_{DL} = (aOh^{-b} + c)We^{-d} + e$. Through least-squares regression, the empirical correlation of T_{DL} as a function of We and Oh (within a $\pm 10\%$ confidence interval; refer to the cyan shaded region in Figure 9) is attained as follows: $T_{DL} = 18 + (16.5Oh^{-0.45} + 160)We^{-0.15}$. Although the percentage of the confidence interval is significant, we believe that this empirical correlation will provide an approximated reference value for future researchers in this field, especially for engineering research and developmental activities in the domain.

3.5. Residence Time of the Droplets at T_{DL} . The nondimensional residence time (t_r^*) of the droplets during the Leidenfrost state of different test fluids, i.e., at T_{DL} is illustrated in Figure 7. We defined the nondimensional residence time ($t_r^* = t_r/t_i$) as the ratio of residence time (t_r) to the impact time ($t_i = D_0/U_0$), where D_0 and U_0 represent the reimpact droplet diameter and impact velocity, respectively. The residence time (t_r) is calculated from the moment of droplet impact to the onset of lift-off. Figure 10a illustrates the temporal snapshots of the nondimensional residence time of different concentrations of NB fluid droplets at almost the same We during their corresponding dynamic Leidenfrost stage. In Figure 10b, it has been observed that for nearly the same We , the nondimensional residence time (t_r^*) decreases with increasing NB concentration. In Figure 8a, it is observed that the T_{DL} decreases with increasing NB concentration for the same We . Since a higher substrate temperature indicates a faster heat transfer rate, it is expected that t_r^* decreases with increasing NB concentration. We scaled the nondimensional residence time (t_r^*) from the experimental data points with respect to We as $t_r^* \approx We^{0.75}$. For a given NB fluid, with increasing We , the T_{DL} is lowered. Consequently, at lower T_{DL} , a lower heat transfer rate results in longer residence times with increasing We .

3.6. Bubble Coalescence during the Leidenfrost Regime ($T_s \approx T_{DL}$). In this section, we have highlighted the bubble coalescence process during the dynamic Leidenfrost stage, i.e., at T_{DL} . Figure 11 illustrates the coalescence of nanobubbles into a macrobubble within the droplet during the Leidenfrost stage (at T_{DL}). At the moment of impact, the dissolved nanobubbles are not traceable by high-speed photography (Figure 11, first column) as it is not possible to resolve the nanoscale dimensions using the conventional optical lens. Columnwise visual inspection reveals that nanobubbles start to coalesce from the onset of the retraction stage (Figure 11, third column, second row onward) as millimeter-size bubbles. Multiple bubbles on the order of millimeters start to emerge from the fourth column onward. It must be noted that the DI water droplets (Figure 11, first row) do not show any such emergence of macrobubbles as they are nearly devoid of dissolved gases. The lifetime of these macrobubbles is more than ~ 100 ms. The emergence of macrobubbles was also observed in drops with dissolved gas components at 300 °C.⁴⁷ However, water droplets containing additives such as polymers or surfactants^{14,16} with negligible dissolved gas exhibited no such macrobubbles to the best of our knowledge. Such rotation of droplets during the Leidenfrost-induced hovering stage was previously observed in the case of water⁴⁸ and polymer droplets.¹³

To emphasize the transformation of nanobubbles into macrobubbles through microbubble coalescence within the droplet during the dynamic Leidenfrost stage, multiple rebounding stages of the liquid droplet (stages I, III, and V in Figure 11 signify the first, third, and fifth rebounds) during both retraction and levitation stages, with their corresponding time frames, have been illustrated in Figure 11. The stages have been sequentially distinguished as nanobubble activation, microbubble formation, microbubble coalescence, and macrobubble formation. In Figure 11, it was noted that the rate of microbubble coalescence increases with an increase in NB concentration due to the great variation in their respective T_{DL} values. It has also been observed that the fluid droplet with lower nanobubble concentration attains macrobubble for-

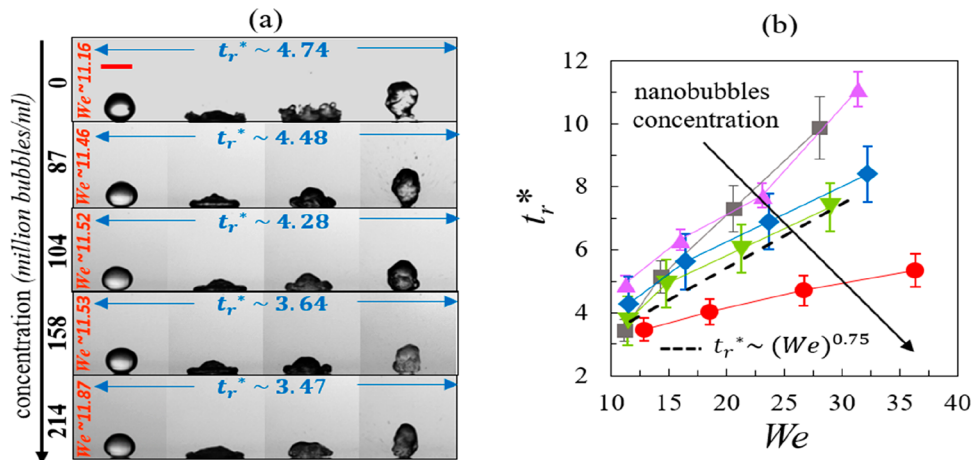


Figure 10. Nondimensional residence time of different concentrations of nanobubble-dissolved water droplets: (a) side view snapshots for varied bubble concentrations at almost the same We and (b) over different Weber (We) numbers, respectively. (b) Symbols ■, ▲, ▼, ♦, and ● represent different bubble concentrations of 0 (water), 87, 104, 158, and 214 million bubbles/mL, respectively. The downward arrow indicates increasing NB concentration.

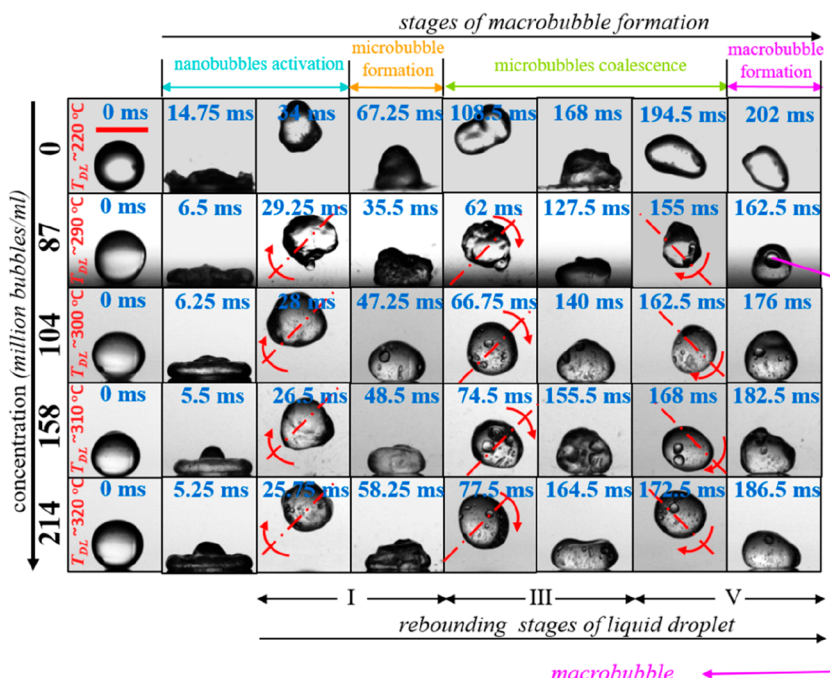


Figure 11. Transformation of nanobubbles into macrobubbles through microbubble coalescence inside a liquid droplet during the dynamic Leidenfrost stage (i.e., at T_{DL}) at a fixed impact velocity of $U = 0.5$ m/s. The scale bar represents 2.64 mm and is the same for all figures. The first row (0 million bubbles/mL) represents deionized water droplets, and the nanobubble concentration increases from the top to bottom rows.

mation in a relatively short time compared to that for higher nanobubble concentration.

3.7. Droplet Rebound Dynamics at T_{DL} . The bouncing dynamics of the droplets with different NB concentrations during the Leidenfrost state is illustrated in Figure 12. The bouncing dynamics is characterized by the nondimensional rebound height (h_{max}/R), which is the ratio of the maximum rebound height of the droplet to its preimpact radius. It is readily evident that the nondimensional rebound height (h_{max}/R) for a fixed impact velocity decreases with an increase in NB concentration. In the case of DI water droplets, the bouncing height increases with impact velocity. On the contrary, for the droplets of NB fluids, the nondimensional rebound height decreases with increased impact velocity.

3.8. Effect of Impact Momentum in the Post-Leidenfrost Regime ($T_s \approx 400$ °C) > T_{DL} . Next, we present the dependence of impact velocity (impact momentum) on various rebound behaviors during the impact of NB droplets at a fixed superheated substrate temperature (i.e., $T_s \approx 400$ °C > T_{DL}) in Figure 13. The representative NB fluid has a concentration of 87 million bubbles/mL. At low impact velocity ($U = 0.5$ m/s), the droplet rebounds and stays intact without any indication of splashing. This behavior was called the rebounding Leidenfrost state. At slightly higher impact velocities (i.e., $U = 0.625$ and 0.75 m/s), drop rebound was observed along with the spraylike ejection of secondary droplets. This behavior was called the spraying Leidenfrost state. With further increases in impact velocity ($U = 0.875$ m/

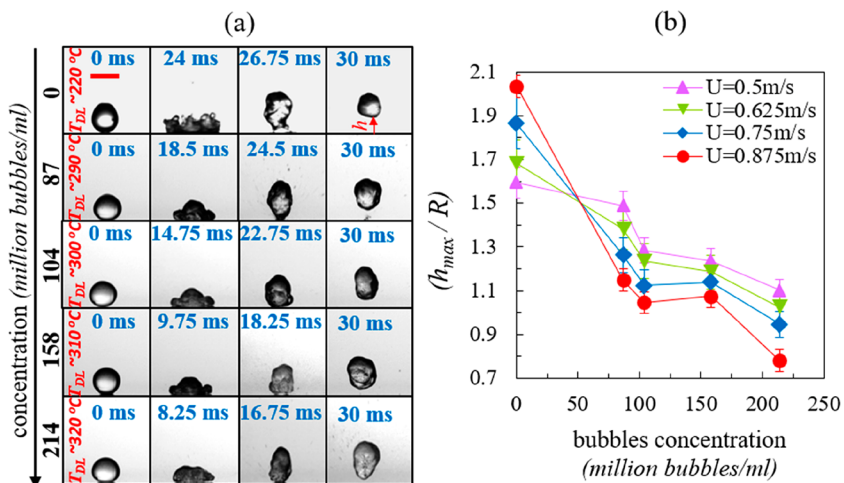


Figure 12. Maximum nondimensional rebound height (h_{max}/R) of different concentrations of nanobubble-dispersed droplets during the dynamic Leidenfrost stage: (a) side view snapshots for varied bubble concentrations at an impact velocity of $U = 0.5 \text{ m/s}$ and (b) maximum nondimensional rebound height (h_{max}/R), respectively.

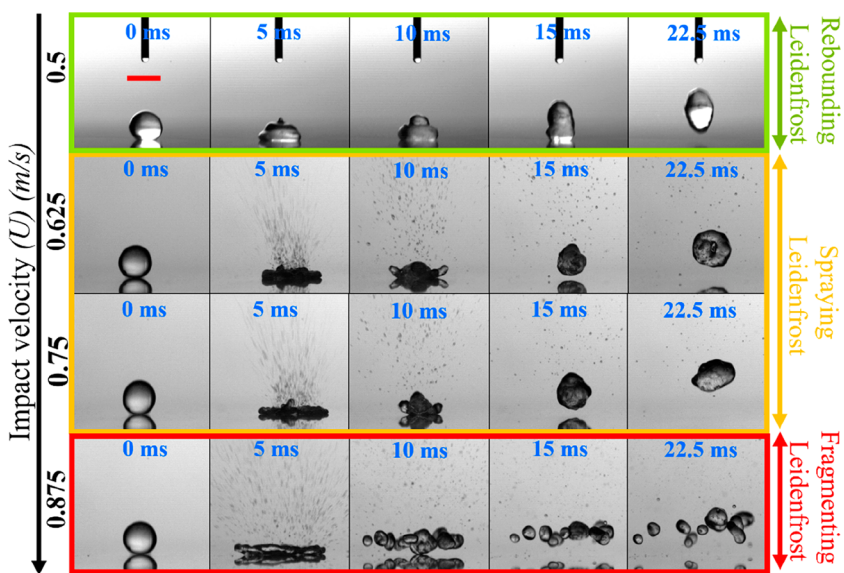


Figure 13. Impact velocity dependence on different Leidenfrost states of nanobubble-dispersed fluid droplets with a particular concentration (87 million bubbles/mL) at a fixed elevated substrate temperature of $T_s \approx 400 \text{ }^\circ\text{C}$. Videos are provided as Supporting Information for observation of the temporal dynamics at different speeds: [Video S4](#) (first row 0.5 m/s), [Video S6](#) (second row 0.625 m/s), [Video S5](#) (third row 0.75 m/s), and [Video S7](#) (fourth row 0.875 m/s).

s), droplets undergo fragmentation into smaller droplets during the retraction process. This state was called the fragmenting Leidenfrost stage. The regime maps of these behaviors as a function of We and substrate temperature are discussed in the next section (Figure 14).

3.9. Boiling Regime Map. Finally, Figure 14a,b represents the phase diagram of different boiling regimes of DI water and NB fluid droplets, respectively, as a function of We and substrate temperature. The highest concentration of NB, i.e., 214 million bubbles/mL was chosen as the representative fluid. The various boiling regimes are distinguished as the CCR mode (I), transition boiling (II), rebounding Leidenfrost state (III), spraying Leidenfrost state (IV), and fragmentation Leidenfrost state (V). In contrast to DI water droplets, NB fluid drops witness the emergence of the CCR mode (I) and spraying Leidenfrost state (IV). In addition, the regime (II) of transition boiling is much larger in the case of NB fluids due to

a higher T_{DL} than for DI water drops. The demarcation zone between II and III for both water and NB fluids suggests that T_{DL} is decreasing with We , reminiscent of Figure 7a.

Similarly, the Leidenfrost (bounce-off nature of the impacting parent droplet) state has been distinguished as the rebounding Leidenfrost state (III), spraying Leidenfrost state (IV), and fragmentation Leidenfrost state (V). In this context, it is noteworthy to discuss the contrasting phase regimes of transition boiling (II) and the fragmenting Leidenfrost state (V) in water and NB fluid. Due to the CCR mode in NB fluids, the transition boiling occurs at lower temperature ($150 \text{ }^\circ\text{C}$) only in the case of high We (~40). Similarly, in comparison to water, fragmentation boiling in the case of NB fluids is happening at a much higher We . This happens due to the emergence of regime (IV) in NB fluids.

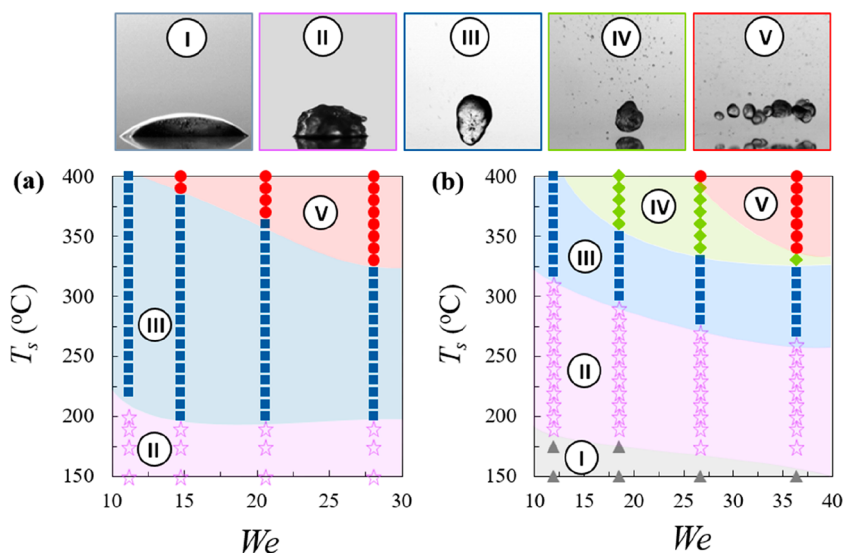


Figure 14. Phase map of boiling regimes of impacting droplets with varied Weber (We) numbers of (a) deionized water and (b) NB fluid (concentration of 214 million bubbles/mL) drops. The top row shows representative snapshots of the different boiling behaviors.

4. CONCLUSIONS

This article presents a novel method for enhancing the dynamic Leidenfrost phenomenon by using nanobubble-dispersed fluid droplets. We note that the NB droplets show a variety of phenomenology during boiling in the pre- and post-Leidenfrost regimes. It was shown that for a given impact velocity the T_{DL} increases with increasing NB concentration, and the NB fluids delay the Leidenfrost effect by significant amounts. The empirical correlation of T_{DL} ($T_{DL} \approx We^{-0.15}$ and $Oh^{-0.45}$) were developed with experimental data points in the form of nondimensional numbers such as the Weber number (We) and Ohnesorge number (Oh). We have shown that rewetting due to the presence of the dispersed NBs and possible formation of a microscale gas layer between the solid–liquid interface could be crucial mechanisms for the delayed Leidenfrost state. Finally, we have demarcated the different boiling regimes of impacting nanobubble-dispersed fluid droplets through regime phase maps as a function of the Weber number (We) and substrate temperature (T_s). The emergence of regimes such as the CCR (constant contact radius) mode and the spraying Leidenfrost state was observed in the case of NB fluids. We believe that our findings will encourage future researchers and developers to explore the potential use of NB fluids in the thermal management of high-temperature devices and components.

■ ASSOCIATED CONTENT

Data Availability Statement

All data pertaining to this research work is available in the manuscript.

■ Supporting Information

The Supporting Information is available free of charge at <https://pubs.acs.org/doi/10.1021/acs.langmuir.2c01891>.

Video S1: Temporal evolution of the nanobubble fluid (104 million bubbles/mL) droplet during contact boiling stage, i.e., at ($T_s \approx 150^\circ\text{C}$) $< T_{DL}$ at a fixed impact velocity of $U = 0.5 \text{ m/s}$ (MP4)

Video S2: Temporal evolution of the water droplet during contact boiling stage, i.e., at ($T_s \approx 150^\circ\text{C}$) $< T_{DL}$ at a fixed impact velocity of $U = 0.5 \text{ m/s}$ (MP4)

Video S3: Transition boiling stage, i.e., at ($T_s \approx 190^\circ\text{C}$) $< T_{DL}$ at a fixed impact velocity of $U = 0.5 \text{ m/s}$ of a nanobubble droplet (104 million bubbles/mL) (MP4)

Video S4: Rebounding Leidenfrost states of nanobubbles fluid droplets (87 million bubbles/mL) at a fixed elevated substrate temperature of $T_s \approx 400^\circ\text{C}$ with an impact velocity of 0.5 m/s (MP4)

Video S5: Boiling of nanobubbles fluid droplets (87 million bubbles/mL) at a fixed elevated substrate temperature of $T_s \approx 400^\circ\text{C}$ with an impact velocity of 0.75 m/s (MP4)

Video S6: Boiling of nanobubbles fluid droplets (87 million bubbles/mL) at a fixed elevated substrate temperature of $T_s \approx 400^\circ\text{C}$ with an impact velocity of 0.625 m/s (MP4)

Video S7: Boiling of nanobubbles fluid droplets (87 million bubbles/mL) at a fixed elevated substrate temperature of $T_s \approx 400^\circ\text{C}$ with an impact velocity of 0.875 m/s (MP4)

■ AUTHOR INFORMATION

Corresponding Authors

Purbarun Dhar – *Hydrodynamics and Thermal Multiphysics Lab (HTML), Department of Mechanical Engineering, Indian Institute of Technology Kharagpur, West Bengal 721302, India; [ORCID](https://orcid.org/0000-0001-5473-2993); Phone: +91-3222-28-2938; Email: purbarun@mech.iitkgp.ac.in*

Devranjan Samanta – *Department of Mechanical Engineering, Indian Institute of Technology Ropar, Punjab 140001, India; [ORCID](https://orcid.org/0000-0002-3406-1472); Phone: +91-1881-24-2109; Email: devranjan.samanta@iitrpr.ac.in*

Authors

Gudlavalleti V V S Vara Prasad – *Department of Mechanical Engineering, Indian Institute of Technology Ropar, Punjab 140001, India*

Harsh Sharma – *Department of Chemical Engineering, Indian Institute of Technology Ropar, Punjab 140001, India*

Neelkanth Nirmalkar – *Department of Chemical Engineering, Indian Institute of Technology Ropar, Punjab 140001, India*

Complete contact information is available at:
<https://pubs.acs.org/10.1021/acs.langmuir.2c01891>

Notes

The authors declare no competing financial interest.

ACKNOWLEDGMENTS

G.V.V.S.V.P. thanks the Ministry of Education, government of India, for the doctoral scholarship. D.S. thanks IIT Ropar for partially funding this work (vide grant 9-246/2016/IITRPR/144). P.D. thanks IIT Kharagpur (vide grant SFI) and the Science and Engineering Research Board (SERB) (vide grant SRG/2020/000004) for partially funding this work.

REFERENCES

- (1) Quéré, D. Leidenfrost Dynamics. *Annu. Rev. Fluid Mech.* **2013**, *45* (1), 197–215.
- (2) Liang, G.; Mudawar, I. Review of drop impact on heated walls. *Int. J. Heat Mass Transfer* **2017**, *106*, 103–126.
- (3) Leidenfrost, J. *G. De Aquae Communis Nonnullis Qualitatibus Tractatus*; Ovenius, 1756.
- (4) Visaria, M.; Mudawar, I. Application of Two-Phase Spray Cooling for Thermal Management of Electronic Devices. *IEEE Transactions on Components and Packaging Technologies* **2009**, *32* (4), 784–793.
- (5) Pasandideh-Fard, M.; Aziz, S. D.; Chandra, S.; Mostaghimi, J. Cooling effectiveness of a water drop impinging on a hot surface. *International Journal of Heat and Fluid Flow* **2001**, *22* (2), 201–210.
- (6) Vakarelski, I. U.; Berry, J. D.; Chan, D. Y. C.; Thoroddsen, S. T. Leidenfrost Vapor Layers Reduce Drag without the Crisis in High Viscosity Liquids. *Phys. Rev. Lett.* **2016**, *117*(11), DOI: [10.1103/PhysRevLett.117.114503](https://doi.org/10.1103/PhysRevLett.117.114503).
- (7) Linke, H.; et al. Self-Propelled Leidenfrost Droplets. *Phys. Rev. Lett.* **2006**, DOI: [10.1103/PhysRevLett.96.154502](https://doi.org/10.1103/PhysRevLett.96.154502).
- (8) Bouillant, A.; Mouterde, T.; Bourrienne, P.; Lagarde, A.; Clanet, C.; Quéré, D. Leidenfrost wheels. *Nat. Phys.* **2018**, *14* (12), 1188–1192.
- (9) Tam, D.; von Arnim, V.; McKinley, G. H.; Hosoi, A. E. Marangoni convection in droplets on superhydrophobic surfaces. *J. Fluid Mech.* **2009**, *624*, 101–123.
- (10) Bouillant, A.; Cohen, C.; Clanet, C.; Quéré, D. Self-excitation of Leidenfrost drops and consequences on their stability. *Proc. Natl. Acad. Sci. U. S. A.* **2021**, *118* (26), e2021691118.
- (11) Tran, T.; Staat, H. J. J.; Prosperetti, A.; Sun, C.; Lohse, D. Drop Impact on Superheated Surfaces. *Phys. Rev. Lett.* **2012**, *108*(3), DOI: [10.1103/PhysRevLett.108.036101](https://doi.org/10.1103/PhysRevLett.108.036101).
- (12) Bertola, V. An experimental study of bouncing Leidenfrost drops: Comparison between Newtonian and viscoelastic liquids. *Int. J. Heat Mass Transfer* **2009**, *52*(7–8), 1786–1793.
- (13) Dhar, P.; Mishra, S. R.; Gairola, A.; Samanta, D. Delayed Leidenfrost phenomenon during impact of elastic fluid droplets. *Proceedings of the Royal Society A: Mathematical, Physical and Engineering Sciences* **2020**, *476* (2243), 20200556.
- (14) Chen, H.; Cheng, W.-l.; Peng, Y.-h.; Jiang, L.-j. Dynamic Leidenfrost temperature increase of impacting droplets containing high-alcohol surfactant. *Int. J. Heat Mass Transfer* **2018**, *118*, 1160–1168.
- (15) Prasad, G. V. V.; Dhar, P.; Samanta, D. Postponement of dynamic Leidenfrost phenomenon during droplet impact of surfactant solutions. *Int. J. Heat Mass Transfer* **2022**, *189*, 122675.
- (16) Paul, G.; Das, P. K.; Manna, I. Nanoparticle deposition from nanofluid droplets during Leidenfrost phenomenon and consequent rise in transition temperature. *Int. J. Heat Mass Transfer* **2020**, *148*, 119110.
- (17) Jollans, T.; Orrit, M. Explosive, oscillatory, and Leidenfrost boiling at the nanoscale. *Phys. Rev. E* **2019**, *99* (6), DOI: [10.1103/PhysRevE.99.063110](https://doi.org/10.1103/PhysRevE.99.063110).
- (18) Kruse, C.; et al. Extraordinary Shifts of the Leidenfrost Temperature from Multiscale Micro/Nanostructured Surfaces. *Langmuir* **2013**, *29* (31), 9798–9806.
- (19) Jiang, M.; et al. Inhibiting the Leidenfrost effect above 1,000 °C for sustained thermal cooling. *Nature* **2022**, *601* (7894), 568–572.
- (20) Celestini, F.; Kirstetter, G. Effect of an electric field on a Leidenfrost droplet. *Soft Matter* **2012**, *8* (22), 5992.
- (21) Nirmalkar, N.; Pacek, A. W.; Barigou, M. On the Existence and Stability of Bulk Nanobubbles. *Langmuir* **2018**, *34* (37), 10964–10973.
- (22) Nirmalkar, N.; Pacek, A. W.; Barigou, M. Interpreting the interfacial and colloidal stability of bulk nanobubbles. *Soft Matter* **2018**, *14* (47), 9643–9656.
- (23) Nirmalkar, N.; Pacek, A. W.; Barigou, M. Bulk Nanobubbles from Acoustically Cavitating Aqueous Organic Solvent Mixtures. *Langmuir* **2019**, *35* (6), 2188–2195.
- (24) Weijns, J. H.; Seddon, J. R. T.; Lohse, D. Diffusive Shielding Stabilizes Bulk Nanobubble Clusters. *ChemPhysChem* **2012**, *13* (8), 2197–2204.
- (25) Tan, B. H.; An, H.; Ohl, C.-D. How Bulk Nanobubbles Might Survive. *Phys. Rev. Lett.* **2020**, *124*(13) DOI: [10.1103/PhysRevLett.124.134503](https://doi.org/10.1103/PhysRevLett.124.134503).
- (26) Epstein, P. S.; Plesset, M. S. Erratum: On the Stability of Gas Bubbles in Liquid-Gas Solutions. *J. Chem. Phys.* **1951**, *19* (2), 256.
- (27) Babu, K. S.; Amamcharla, J. K. Generation methods, stability, detection techniques, and applications of bulk nanobubbles in agro-food industries: a review and future perspective. *Critical Reviews in Food Science and Nutrition* **2022**, 1–20.
- (28) Alheshibri, M.; Qian, J.; Jehannin, M.; Craig, V. S. J. A History of Nanobubbles. *Langmuir* **2016**, *32* (43), 11086–11100.
- (29) Agarwal, A.; Ng, W. J.; Liu, Y. Principle and applications of microbubble and nanobubble technology for water treatment. *Chemosphere* **2011**, *84* (9), 1175–1180.
- (30) Fan, X.; et al. Ultrasonic Nanobubbles Carrying Anti-PSMA Nanobody: Construction and Application in Prostate Cancer-Targeted Imaging. *PLoS One* **2015**, *10*(6), e0127419.
- (31) Misra, S. K.; et al. Trimodal Therapy: Combining Hyperthermia with Repurposed Bexarotene and Ultrasound for Treating Liver Cancer. *ACS Nano* **2015**, *9* (11), 10695–10718.
- (32) Ushida, A.; Hasegawa, T.; Nakajima, T.; Uchiyama, H.; Narumi, T. Drag reduction effect of nanobubble mixture flows through micro-orifices and capillaries. *Experimental Thermal and Fluid Science* **2012**, *39*, 54–59.
- (33) Ebina, K. Oxygen and Air Nanobubble Water Solution Promote the Growth of Plants, Fishes, and Mice. *PLoS One* **2013**, *8* (6), e65339.
- (34) Liu, S.; Oshita, S.; Makino, Y.; Wang, Q.; Kawagoe, Y.; Uchida, T. Oxidative Capacity of Nanobubbles and Its Effect on Seed Germination. *ACS Sustainable Chem. Eng.* **2016**, *4* (3), 1347–1353.
- (35) Matsuki, N.; Ishikawa, T.; Ichiba, S.; Shiba, N.; Ujike, Y.; Yamaguchi, T. Oxygen supersaturated fluid using fine micro/nanobubbles. *Int. J. Nanomed.* **2014**, 4495.
- (36) Vara Prasad, G. V. V. S.; Dhar, P.; Samanta, D. Magneto-Elastic Effect in Non-Newtonian Ferrofluid Droplets Impacting Superhydrophobic Surfaces. *Langmuir* **2021**, *37* (32), 9673–9682.
- (37) Sharma, H.; Nirmalkar, N. Enhanced gas-liquid mass transfer coefficient by bulk nanobubbles in water. *Materials Today: Proceedings* **2022**, *57*, 1838–1841.
- (38) Agarwal, K.; Trivedi, M.; Nirmalkar, N. Does salting-out effect nucleate nanobubbles in water: Spontaneous nucleation? *Ultrasonics Sonochemistry* **2022**, *82*, 105860.
- (39) Van Gaalen, R. T.; Wijhoff, H. M. A.; Kuerten, J. G. M.; Diddens, C. Competition between thermal and surfactant-induced Marangoni flow in evaporating sessile droplets. *J. Colloid Interface Sci.* **2022**, *622*, 892–903.
- (40) Vega-Sánchez, C.; Peppou-Chapman, S.; Zhu, L.; Neto, C. Nanobubbles explain the large slip observed on lubricant-infused surfaces. *Nat. Commun.* **2022**, *13*(1), DOI: [10.1038/s41467-022-28016-1](https://doi.org/10.1038/s41467-022-28016-1).

- (41) Kaushal, A.; Jaiswal, V.; Mehandia, V.; Dhar, P. Competing thermal and solutal advection decelerates droplet evaporation on heated surfaces. *European Journal of Mechanics - B/Fluids* **2022**, *91*, 129–140.
- (42) Yu, D. I.; et al. Dynamics of Contact Line Depinning during Droplet Evaporation Based on Thermodynamics. *Langmuir* **2015**, *31* (6), 1950–1957.
- (43) Shaikeea, A. J. D.; Basu, S.; Tyagi, A.; Sharma, S.; Hans, R.; Bansal, L. Universal representations of evaporation modes in sessile droplets. *PLoS One* **2017**, *12*(9), e0184997.
- (44) Panchanathan, D.; Bourrianne, P.; Nicollier, P.; Chottratanapituk, A.; Varanasi, K. K.; McKinley, G. H. Levitation of fuzzy drops. *Science Advances* **2021**, *7*(28), DOI: 10.1126/sciadv.abf0888.
- (45) Jeschar, R.; Kraushaar, H.; Griebel, H. Influence of gases dissolved in cooling water on heat transfer during stable film boiling. *Steel Research* **1996**, *67* (6), 227–234.
- (46) Khavari, M.; Tran, T. Universality of oscillating boiling in Leidenfrost transition. *Phys. Rev. E* **2017**, *96*(4), DOI: 10.1103/PhysRevE.96.043102.
- (47) Cui, Q.; Chandra, S.; McCahan, S. The Effect of Dissolving Gases or Solids in Water Droplets Boiling on a Hot Surface. *Journal of Heat Transfer* **2001**, *123* (4), 719–728.
- (48) Chen, S.; Bertola, V. Jumps, somersaults, symmetry breaking in Leidenfrost drops. *Phys. Rev. E* **2016**, DOI: 10.1103/PhysRevE.94.021102.

□ Recommended by ACS

Study on the Bouncing Behaviors of a Non-Newtonian Fluid Droplet Impacting on a Hydrophobic Surface

Hailong Liu, Junfeng Wang, et al.

MARCH 10, 2023

LANGMUIR

READ ↗

Energy Loss for Droplets Bouncing Off Superhydrophobic Surfaces

Calvin Thenarianto, Dan Daniel, et al.

FEBRUARY 16, 2023

LANGMUIR

READ ↗

Electrically Manipulated Vapor Condensation on the Dimpled Surface: Insights from Molecular Dynamics Simulations

Shao-Yu Wang, Duu-Jong Lee, et al.

JANUARY 03, 2023

LANGMUIR

READ ↗

Experimental Investigation of Dropwise Condensation Shedding by Shearing Airflow in Microgravity Using Different Surface Coatings

Milad Shakeri Bonab, Alidad Amirfazli, et al.

DECEMBER 27, 2022

LANGMUIR

READ ↗

Get More Suggestions >